




# SAR Interferometry Infrastructure Deformation Monitoring by the Number of Redundant Observations Optimizes Phase Unwrapping Networks

Baohang Wang , Chaoying Zhao , Senior Member, IEEE, Qin Zhang , Member, IEEE, Chengsheng Yang, Wenhong Li, Guangrong Li, Ya Kang, and Shouzhu Zheng

**Abstract**—This work employs synthetic aperture radar interferometry technology to investigate infrastructure deformation in which discontinuous and irregular interferometric fringes make phase unwrapping (PhU) challenging. This study aimed to improve the reliability and practicability of PhU through the number of redundant observations to optimize PhU networks. The proposed PhU networks optimization strategy can improve the efficiency of PhU and accuracy. In addition, we evaluated the reliability of selected networks based on two popular methods. Finally, we used the Edgelist PhU method to demonstrate the reliability of optimized networks. Experiments were carried out on the Nanjing Dashengguan Yangtze River high-speed railway bridge, China, and on buildings deformation in Xi'an, China, the results of which indicate that the proposed method can effectively balance the accuracy and efficiency of PhU.

**Index Terms**—Infrastructure, number of redundant observations (NRO), phase unwrapping (PhU), quality evaluation, synthetic aperture radar interferometry (InSAR).

## I. INTRODUCTION

**S**YNTHETIC aperture radar interferometry (InSAR) technology is a repeated measurement technique with the advantages of a large spatial scale, low cost, high accuracy, and continuous observability [1]. As buildings age, artificial structures gradually deteriorate, which may result in structural collapse and

personal and economic losses [2]. InSAR technology has been applied to analyze infrastructures, such as buildings, bridges, and highways [3], [4], [5], [6], [7]. Interference phase quality is typically guaranteed in artificial buildings. However, digital elevation model (DEM) errors and discontinuous and irregular interferometric fringes pose challenges for phase unwrapping (PhU). The accuracy of PhU directly affects the accuracy of InSAR products.

In conventional permanent scatterer (PS) InSAR technology [8], deformation parameters are retrieved through a predefined deformation model (e.g., DEM error and linear deformation rate) and PhU is then performed for the residual phase in space. Similarly, the periodogram analysis method [8], linear regression analysis method [9], weighted periodogram with small baseline (SB) interferograms [10], integer least squares (LS) method [11], and LS with the phase ambiguity detector method [12] have been proposed. Monserrat et al. [13] introduced a thermal expansion deformation component into the InSAR phase model to monitor building deformation. Costantini et al. [14] proposed the permanent scatterer pair (PSP) method, which identifies arcs that satisfy a predefined phase model instead of selecting point targets. These methods are used to estimate deformation parameters by stacking interferograms and a predefined deformation model.

With respect to spatial PhU strategies, global optimization approaches, such as the minimum cost flow (MCF) algorithm [15] and statistical-cost network-flow (SNAPHU) algorithm [16], generally minimize the difference between the unwrapped phase and its original wrapped phase globally. Path-tracking strategies generally integrate the phase gradient field along optimized paths, such as the branch-cut algorithm [17] and region-growing algorithm [18]. Two-tier network [19], [20], hierarchical networking, and constrained adjustment [21] have been introduced into PhU. In addition, artificial intelligence strategies have been applied to PhU [22]. In these methods, only a single interferogram is used to implement PhU.

To avoid unwrapping errors, temporal phase information can be used to promote the spatial PhU, such as the extended MCF method based on 1-D temporal and 2-D spatial PhU [23] and its improved version [24]. The 3-D PhU methods have also

Manuscript received 23 April 2023; revised 9 June 2023 and 3 July 2023; accepted 25 July 2023. Date of publication 31 July 2023; date of current version 9 August 2023. This work was supported in part by the Natural Science Foundation of Fujian Province, China, under Grant 2023J05257 and Grant 2023J011415, in part by the Project of Fujian Educational Bureau Grant JAT220325, and in part by the Initial Scientific Research Fund of Talents in Minjiang University Grant MJY23002. (Corresponding authors: Chaoying Zhao; Qin Zhang.)

Baohang Wang and Shouzhu Zheng are with the College of Geography and Oceanography, Minjiang University, Fuzhou 350108, China (e-mail: wangbaohang@mju.edu.cn; szzheng0304@mju.edu.cn).

Chaoying Zhao, Qin Zhang, Chengsheng Yang, and Guangrong Li are with the College of Geological Engineering and Geomatics, Chang'an University, Xi'an 710054, China (e-mail: cyzhao@chd.edu.cn; dczhangq@chd.edu.cn; yangchengsheng@chd.edu.cn; 2020226022@chd.edu.cn).

Wenhong Li is with the Xi'an Center of Geological Survey, China Geological Survey, Xi'an 710054, China (e-mail: liwenhong01@mail.cgs.gov.cn).

Ya Kang is with the School of Geographic and Biologic Information, Nanjing University of Posts and Telecommunications, Nanjing 210023, China (e-mail: kangya@njupt.edu.cn).

Digital Object Identifier 10.1109/JSTARS.2023.3300097

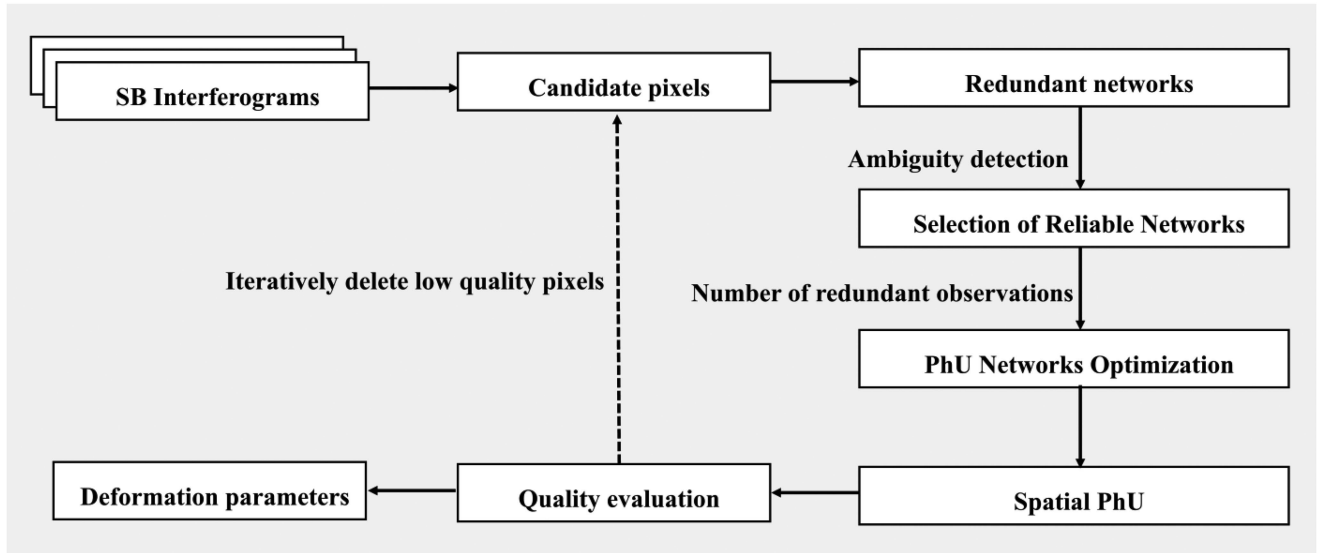


Fig. 1. Flowchart of the proposed method.

been proposed [25]. The null-space algorithm [26] and Bayesian theory algorithm [27] were introduced into PhU. Spatiotemporal network closure constraints [28], a multicomponent temporal coherence model [29], and a triangle-oriented spatiotemporal PhU algorithm [30] have been proposed. An overview of the PhU methods was provided by Yu et al. [31]. These methods aim to improve the reliability of the ambiguity estimation.

Redundant networks can improve the ambiguity estimation and performance of spatial PhU [32]. An ambiguity detection method was used to select reliable arcs from local free networks [33]. The shortest path method was employed to optimize PhU networks [34]. Reliable redundant networks have been used to perform spatial PhU using an edge list algorithm [35], [36]. The  $K$  nearest network was used to encrypt the Delaunay triangular networks for the spatial PhU [37], [38]. However, a large number of redundant networks are uncontrollable, which imposes a burden on the spatial PhU algorithm.

PhU is a key step in infrastructure deformation monitoring in which discontinuous and irregular interferometric fringes pose a challenge. Therefore, after obtaining reliable redundant networks/arcs [33], [35], we suggest using the number of redundant observations (NRO) strategies to optimize these networks, which can improve the efficiency of PhU while ensuring accuracy. In addition, we evaluated the accuracy of the selected reliable redundant networks using ambiguity detection and temporal coherence of double-difference phase methods. Next, we performed spatial PhU by the Edgelist MCF PhU methods [35], [36], [38] to demonstrate the reliability of optimized networks.

Finally, the proposed method was tested using 230 Sentinel-1A/B SAR data points from 2016 to 2022 from the Nanjing Dashengguan Yangtze River high-speed railway bridge in China. The application to building deformation was tested in the land subsidence area of Xi'an, China, using 47 TerraSAR-X datasets from 2011 to 2015.

## II. METHODOLOGY

Fig. 1 shows a flowchart of the proposed method, which starts with SB interferograms. First, we selected candidate pixels to generate redundant networks and to distinguish reliable arcs. Second, we used the NRO strategy to optimize reliable networks. We then performed a quality assessment of the PhU. Finally, we deleted the low-quality pixels and iterated the steps above.

### A. Selection of Reliable Networks

Reliable networks/arcs are a key factor in improving the performance of PhUs. Based on the PSP strategy, reliable arcs are selected from a predefined deformation model [14]. Similarly, the temporal coherence of the double-difference phase ( $\gamma^{p,q}$ ) was employed to select reliable PhU arcs [8], [34], [38] without deformation models, as shown in the following equation:

$$\gamma^{p,q} = \frac{1}{M} \left| \sum_{ifg=1}^M \exp(j\Delta\varphi_{ifg}^{p,q}) \right|$$

$$\Delta\varphi_{ifg}^{p,q} = \text{wrap} \left( \varphi_{ifg}^p - \varphi_{ifg}^q \right) \quad (1)$$

where  $p$  and  $q$  are two neighborhood pixels,  $M$  is the number of all SB interferograms, and  $\Delta\varphi_{ifg}^{p,q}$  is the double-difference phase between pixels  $p$  and  $q$ .

In addition, Zhang et al. [12], Wu et al. [33] proposed an ambiguity detection method to distinguish reliable arcs, which employs LS residuals to identify arcs without ambiguity phase, as shown in the following equation:

$$\mathbf{A}_{M \times N} \Delta \boldsymbol{\theta}_{N \times 1}^{p,q} = \Delta \boldsymbol{\varphi}_{M \times 1}^{p,q}$$

$$\Delta \hat{\boldsymbol{\theta}}_{N \times 1}^{p,q} = \left( \mathbf{A}_{M \times N}^T \mathbf{A}_{M \times N} \right)^{-1} \mathbf{A}_{M \times N}^T \Delta \boldsymbol{\varphi}_{M \times 1}^{p,q}$$

$$\Delta \boldsymbol{\varphi}_{M \times 1}^{p,q} - \mathbf{A}_{M \times N}^{p,q} \Delta \hat{\boldsymbol{\theta}}_{N \times 1}^{p,q} = \boldsymbol{\Delta}^{p,q} \quad (2)$$

where  $\mathbf{A}_{M \times N}$  is the design matrix,  $N$  is the number of SAR data,  $\Delta\hat{\theta}_{N \times 1}^{p,q}$  is the estimated double-difference phase time series between pixels  $p$  and  $q$ , and  $\Delta^{p,q}$  is the double-difference residual phase time series after LS estimation.

We can use  $\max |\Delta^{p,q}| < T_{\text{residual}}$  to select reliable arcs based on the threshold  $T_{\text{residual}} = c\sqrt{\max(\mathbf{Q}_{\text{arc}})} + 2\sqrt{\max(\mathbf{Q}_{\Delta\theta})}$  in which the constant  $c$  may be chosen as 3 or 4 [12].  $\mathbf{Q}_{\Delta\theta}$  is the variance covariance matrix of  $\Delta\hat{\theta}_{N \times 1}^{p,q}$ .  $\mathbf{Q}_{\text{arc}}$  is the noise variance of arc. When the threshold value  $T_{\text{residual}}$  is reached, the arc is regarded as an outlier at 95% confidence level [12].

### B. PhU Network Optimization

Typically, we set the distance between two pixels or  $K$  nearest neighbor pixels to generate redundant candidate networks. To determine optimal networks, we can set a large number of  $K$  values or distance thresholds. Based on these two methods, reliable PhU networks can be selected from redundant candidate networks. After obtaining reliable arcs, the structure of the selected arc networks is unknown. A pixel may connect to too many networks, causing a serious burden for the PhU.

The NRO is a key index in geodetic network adjustment, which determines the reliability of the network adjustment [39], [40]. Inspired by NRO, in this article, we used the NRO of each pixel to optimize these reliable networks, as shown in the following equation:

$$\text{Pixel}_i^{\text{NRO}} < T_{\text{NRO}} \quad (3)$$

where  $\text{Pixel}_i^{\text{NRO}}$  is the NRO of each pixel and  $T_{\text{NRO}}$  is the threshold for optimizing the network structure.

The process of NRO optimization is summarized as follows.

- 1) The first step is to delete isolated pixels or local networks. A large spatial distance or  $K$  nearest neighbor pixel threshold can be used to avoid this scenario.
- 2) The second step is to estimate the NRO of each pixel in the network, which can be easily realized using graph theory.
- 3) The third step is to sort redundant arcs according to their LS residual or temporal coherence of residual.
- 4) We maintain the arcs with the number of  $T_{\text{NRO}}$  with the largest coherence or smallest residual. If the NRO of a pixel was less than the threshold  $T_{\text{NRO}}$ , the connected arcs were not deleted.

The purpose of the proposed NRO strategies is to select the number of arcs linked to each pixel. Selected networks' arcs are with the smallest residual or highest coherence. Regardless of the networks maintaining poor-quality arcs, the probability of discarded poor-quality arcs is higher. Therefore, the NRO-optimizing network strategy can be used to balance accuracy and efficiency. In Delaunay triangulation networks of the conventional MCF, the NRO of each pixel is around 5. Therefore, as for the threshold  $T_{\text{NRO}}$ , the threshold  $T_{\text{NRO}} = 5$  is recommended.

### C. Edgelist MCF PhU and Quality Assessment

The MCF algorithm used Delaunay triangulation networks to obtain triangular closure constraints in space and execute linear programming [15]. However, in selected optimization networks, it is difficult to find triangular constraints in space.

Therefore, we can use the Edgelist MCF method, which employs edge constraints to execute linear programming, as shown in the following equation [35], [36], [38]:

$$\begin{aligned} & \min(f_{1 \times D}^+ \mathbf{K}_{D \times 1}^+ - f_{1 \times D}^- \mathbf{K}_{D \times 1}^-) \\ & \text{s.t. } [\mathbf{C}_{D \times P} \quad -\mathbf{C}_{D \times P} \quad \mathbf{I}_{D \times D} \quad \mathbf{I}_{D \times D}] \begin{bmatrix} \mathbf{L}_{P \times 1}^+ \\ \mathbf{L}_{P \times 1}^- \\ \mathbf{K}_{D \times 1}^+ \\ \mathbf{K}_{D \times 1}^- \end{bmatrix} = \Delta\varphi_{D \times 1}^m \end{aligned}$$

$$\text{with } L^+, L^-, K^+, K^- \in \mathbb{N}^0 \quad (4)$$

where  $\mathbf{C}$  is the coefficient matrix of edges' constraints in space with elements of  $-1, 0,$  and  $1$ , and  $\mathbf{I}$  is the unit matrix.  $D$  is the number of reliable arcs,  $S$  is the number of selected reliable pixels, and  $P$  is the number of selected point targets.  $\Delta\varphi_{K \times 1}^m$  is the double-difference phase of  $D$  reliable arcs in the  $m$ th interferogram.  $\mathbf{L}_{P \times 1}^+$  and  $\mathbf{L}_{P \times 1}^-$ ,  $\mathbf{K}_{D \times 1}^+$ , and  $\mathbf{K}_{D \times 1}^-$  are two slack vectors for point and arcs' ambiguities, respectively.  $\theta_{P \times 1}^m = \mathbf{L}_{P \times 1}^+ - \mathbf{L}_{P \times 1}^-$  represents the PhU in the  $m$ th interferogram.

The PhU error leads to deviations in subsequent deformation parameters. Therefore, it is necessary to evaluate their reliabilities. No difference has been found between the unwrapped phase and the original wrapped phase when using the SNAPHU [26] and MCF [14] methods. Pepe and Lanari [23] proposed to use the temporal coherence of the residual ( $\gamma_{\text{LS}}$ ) to assess the reliability of PhU. The residual from the LS method is used to estimate the deformation time series, as shown in the following equation:

$$\gamma_{\text{LS}} = \frac{1}{M} \left| \sum_{i=1}^M \exp \{j(\theta_{M \times 1} - \mathbf{A}_{M \times N} \bar{\theta}_{N \times 1})\} \right| \quad (5)$$

where  $\mathbf{A}$  is the design matrix from the SB interferograms,  $N$  is the number of SAR,  $\bar{\theta}_{N \times 1}$  is the estimated unwrapped phase time series, and  $\theta_{M \times 1}$  is stacking the unwrapped phases.

For SB interferograms, the unwrapped phase triplet closure is used for PhU correction [38]. Meanwhile, we can use unwrapped phase triplet closure  $\theta_{\text{triplet}}$  to assess the reliability of PhU, as shown in the following equation:

$$\mathbf{C}_{S \times M} \theta_{M \times 1} = \theta_{\text{triplet}} \quad (6)$$

where  $\mathbf{C}_{S \times M}$  is the unwrapped phase triplet design matrix from SB interferograms, and  $S$  is the number of unwrapped phase triplet closures.

## III. STUDY AREA SAR DATASET

The Nanjing Dashengguan Yangtze River Bridge is a high-speed railway bridge that crosses the Yangtze River in Nanjing, Jiangsu Province, China. Significant thermal expansion and contraction deformations have been mapped [41], [42]. We collected 230 Sentinel-1A/B SAR datasets from 2016 to 2022 to test the proposed method. In the experiment, we generated 684 SB interferograms using spatiotemporal baseline thresholds [43] and selected PS pixels using the amplitude dispersion index [8]. Fig. 2(a) shows the average SAR intensity image. Fig. 2(b) shows

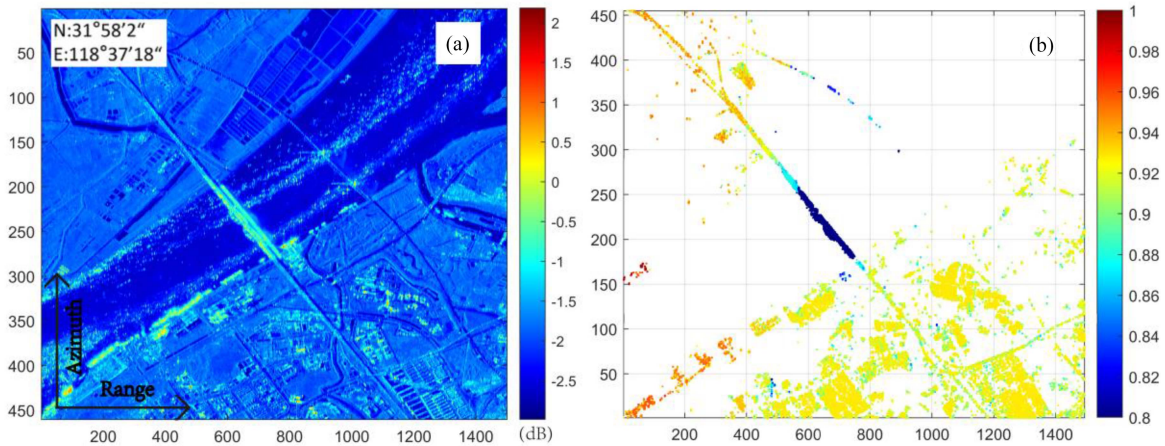


Fig. 2. (a) Average SAR intensity image and (b) temporal coherence of residual.

the temporal coherence of residual in which we used Delaunay triangulation networks to execute PhU by linear programming [15]. It shows that PhU error is severe in the part of the bridge crossing river.

#### IV. RESULTS AND ANALYSIS

##### A. Quality Assessment of Selected Reliable Arcs Based on Different Strategies

We compared the accuracy of the selected reliable arcs for the ambiguity detection method [13], [18], [20] and the temporal coherence of the double-difference phase method [8], [19], [23]. Specifically, we used stacked unwrapped interferograms to compare the reliabilities of the two methods. In the experiment, to avoid isolating the point targets, we set the  $K$  value to 10 000 pixels to generate redundant networks. Next, we set the threshold  $T_{\text{NRO}} = 5$  to optimize the PhU networks.

After spatial Edgelist MCF PhU, we estimated the number of unwrapped phase triplet closure and temporal coherence of residual, as shown in Fig. 3, in which (a and c) and (b and d) are reliable arcs selected by the temporal coherence of double-difference phase and the ambiguity detection method, respectively. Fig. 3(a) and (b) and (c) and (d) are the number of unwrapped phase triplet closure and temporal coherence of residual, respectively.

The PhU results show that the ambiguity detection method can obtain higher temporal coherence of residual and small number of unwrapped phase triangles. Because the temporal coherence of the double-difference phase is an average value in which one or a small number of poor arcs are suppressed. However, ambiguity detection is based on the maximum values of all residuals. Additionally, among the 10 000 nearest redundant arcs in the experimental test, we found the top five arcs with small residual and higher temporal coherence of double-difference phase. In the selection of reliable redundant networks, the ambiguity detection method is based on redundant interferograms. However, the temporal coherence of the double-difference phase method is not.

##### B. NRO PhU Networks Optimization

To demonstrate the reliability of NRO PhU networks optimization, we present four networks using different  $K$  nearest neighbor pixel thresholds (100, 500, 5000, 10 000) in Table I. The number of original pixels is 24 444. The PhU was based on MATLAB R2022b software and 12th Gen Intel(R) Core (TM) i9-12900H 2.50 GHz computer. With the increase of  $K$  nearest neighbor pixel thresholds, the large number of reliable redundant arcs is uncontrollable, which imposes a burden on the Edgelist MCF PhU. Therefore, we used NRO strategies to optimize these networks, which can obtain optimal arcs with preset threshold NRO arcs. After that, we employed four indices to evaluate the performance of the proposed method, including the number of optimized arcs, time consumption, average temporal coherence of residual, and number of unwrapped phase triangles.

As can be seen in Table I, with the increase of  $K$  nearest neighbor pixel thresholds, the number of reliable arcs increase significantly. However, after NRO strategies, the number of optimized arcs can be controlled. Meanwhile, the temporal coherence of residual increase and the number of unwrapped phase triplet closure decrease decline, which shows that the accuracy of PhU has been improved. The results indicate that the proposed NRO strategy can improve the efficiency of PhU while ensuring accuracy.

Meanwhile, we show the number of unwrapped phase triplet closure and temporal coherence of residual as Fig. 4, in which (a and d), (b and e), and (c and f) are corresponding to different  $K$  nearest neighbor pixel thresholds (100, 500, 5000). The top row of Fig. 4 corresponds to the number of unwrapped phase triangles, and the low row of Fig. 4 corresponds to the temporal coherence of the residual.

Fig. 5 shows four optimized spatial arcs, in which (a), (b), (c), and (d) are from different  $K$  nearest neighbor pixel thresholds (100, 500, 5000, and 10 000). It shows that arcs are clustered with small  $K$  nearest neighbor pixel thresholds. In fact, a compromise threshold ( $K$ ) should be selected to generate redundant candidate observations in which we search for optimal networks within local areas.

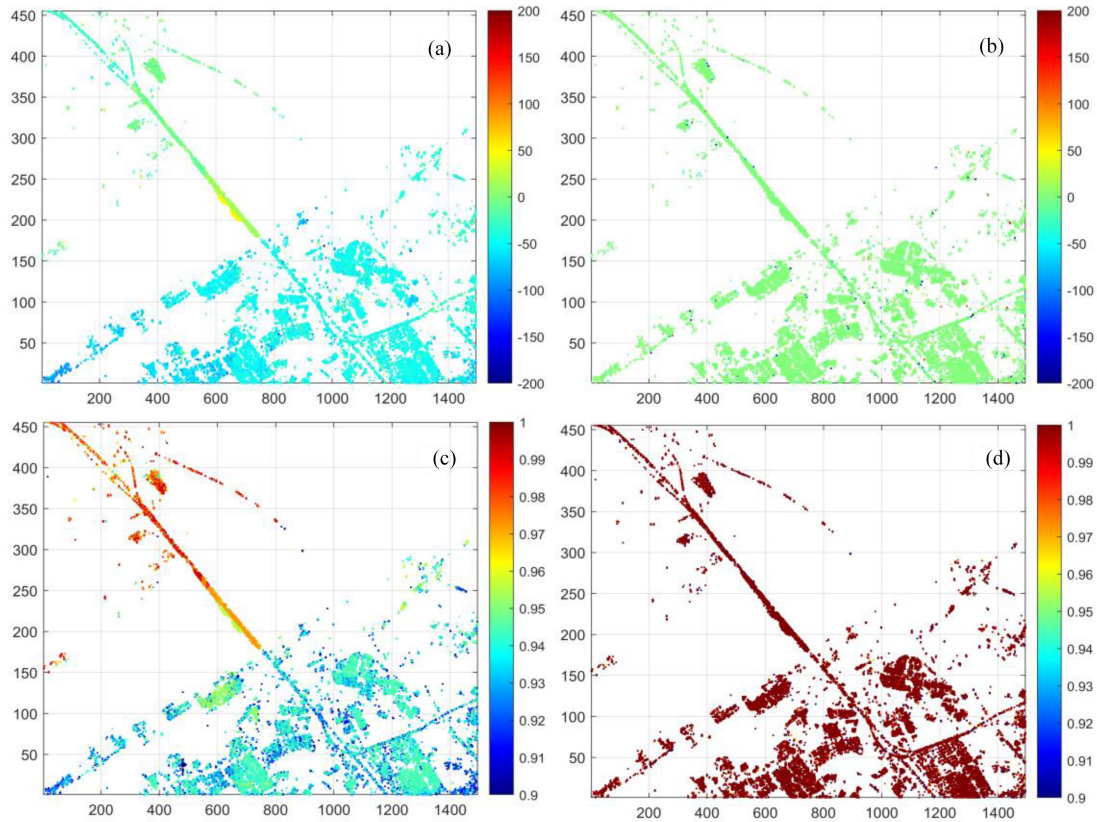


Fig. 3. (a) and (b) show the number of unwrapped phase triplet closures after Edgelist MCF from selected reliable arcs by double-difference phase and temporal coherence of the double-difference phase, respectively; meanwhile, (c) and (d) show the temporal coherence of residual.

TABLE I  
EVALUATION INDICES UNDER DIFFERENT NETWORKS

$K$ nearest neighbor pixel threshold	Number of reliable arcs	Number of optimized arcs by NRO	Time consumption (s)	Average temporal coherence of residual	Number of unwrapped phase triplet closure
10 000	13 744 564	114 574	18.7251	0.9930	53 322
5000	11 039 667	114 167	17.0946	0.9913	63 569
500	6 177 863	122 193	93.7546	0.8535	1 065 822
100	1 209 776	122 056	43.9461	0.8003	1 568 200

However, the large  $K$  nearest neighbor pixel thresholds generated very redundant arcs. After NRO strategies, we obtained approximately the same number of arcs. Therefore, we used NRO strategies to optimize these networks, both improving the efficiency of PhU and ensuring accuracy.

### C. Application to the Nanjing Dashengguan Yangtze River Bridge

Previous research has mainly focused on considerable thermal expansion and contraction deformations of the Nanjing Dashengguan Yangtze River Bridge [41], [42]. However, here, we provide relatively complete deformation characteristics of the Nanjing Dashengguan Yangtze River high-speed railway

bridge and its surrounding environment, rather than just the thermal expansion characteristics of local bridges.

In this experiment, we set the NRO threshold to 5 to optimize PhU networks. The unwrapped 684 interferograms were used to estimate the line of sight (LOS) deformation rate, as shown in Fig. 6(a). Fig. 6(b) and (c) shows the DEM and coefficient of thermal expansion, respectively. The six points in the LOS deformation time series are shown in Fig. 7.

Bridge deformation is mainly temperature-related. The correlation between the deformation time series and temperature exceeds 0.96, as shown in Fig. 7. The deformation time series results show that the Nanjing Dashengguan Yangtze River high-speed railway bridge has different deformation characteristics at different locations along its longitudinal orientation. The maximum deformation was found to be 70 mm in the LOS

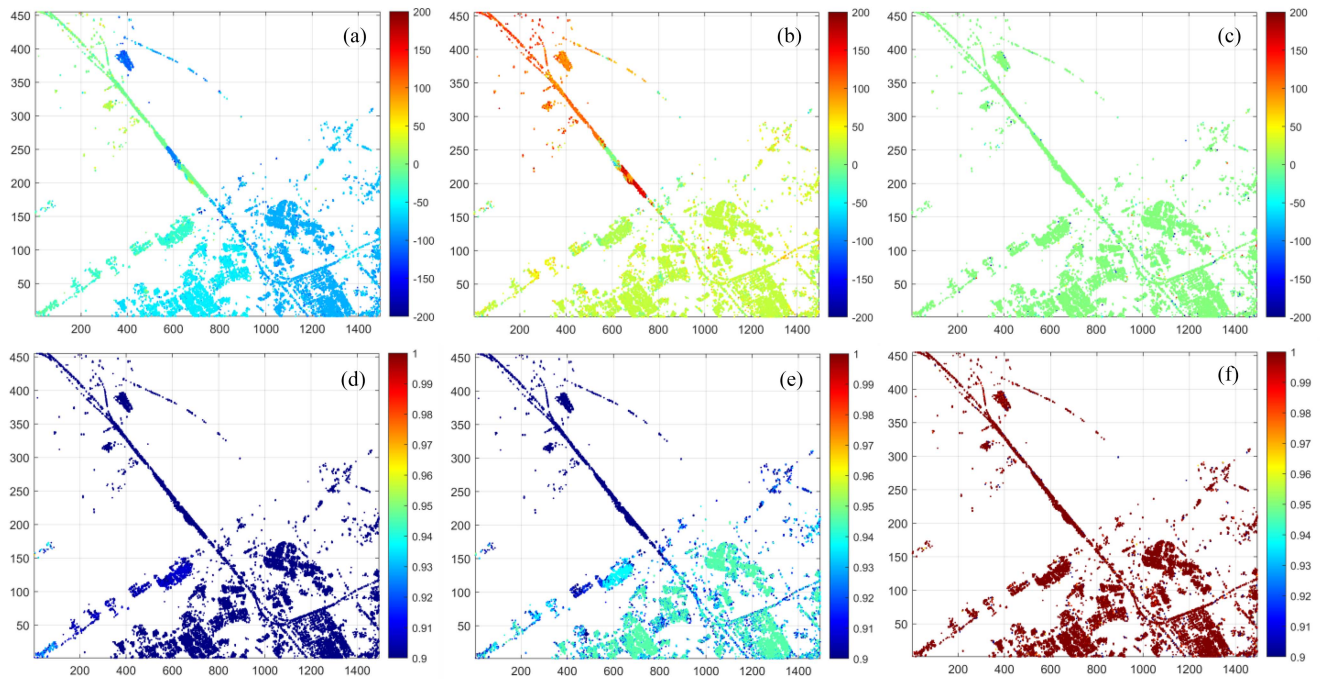


Fig. 4. (a)–(c) Number of unwrapped phase triplet closure and (d)–(f) temporal coherence of residual with different networks, respectively.

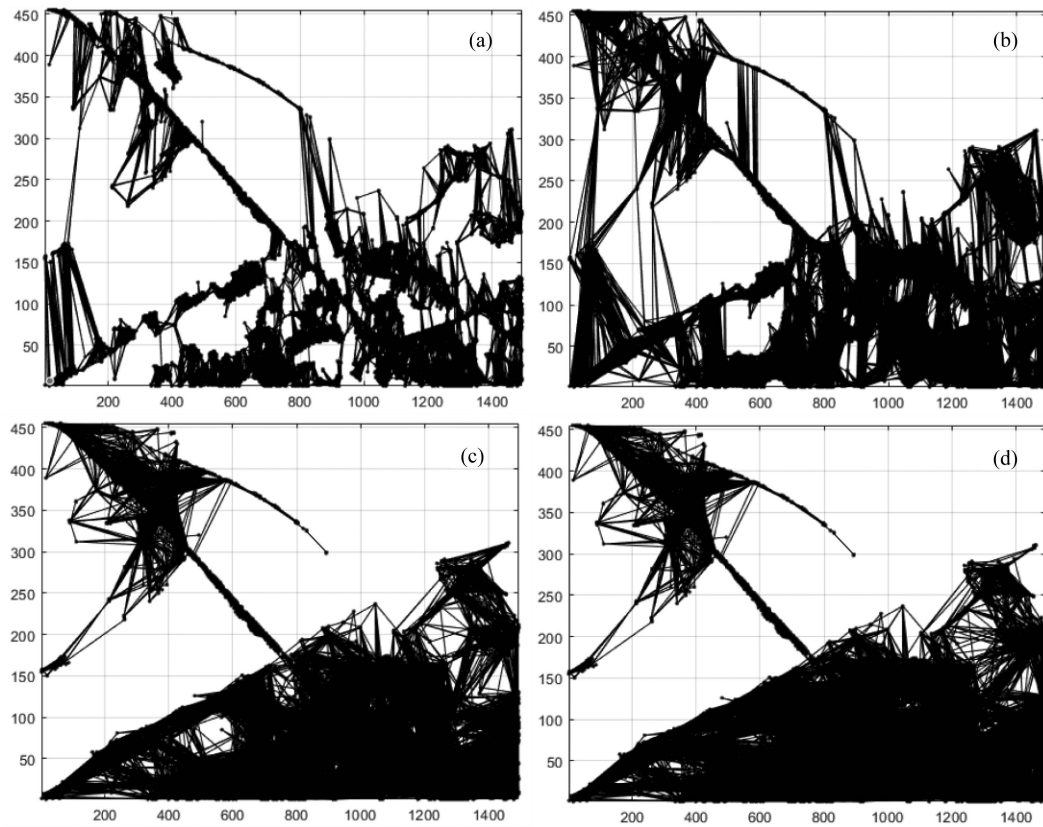


Fig. 5. Optimized PhU networks. (a), (b), (c), and (d) are optimized arcs from different  $K$  nearest neighbor pixel thresholds of 100, 500, 5000, and 10 000, respectively.

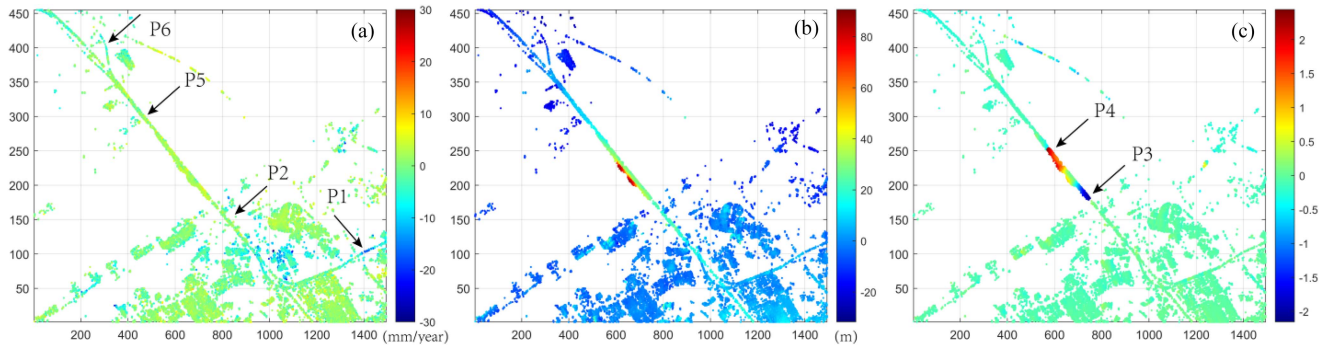


Fig. 6. (a)–(c) Deformation rate, DEM error, and coefficient of thermal expansion, respectively. Points P1–P4 are shown in Fig. 7.

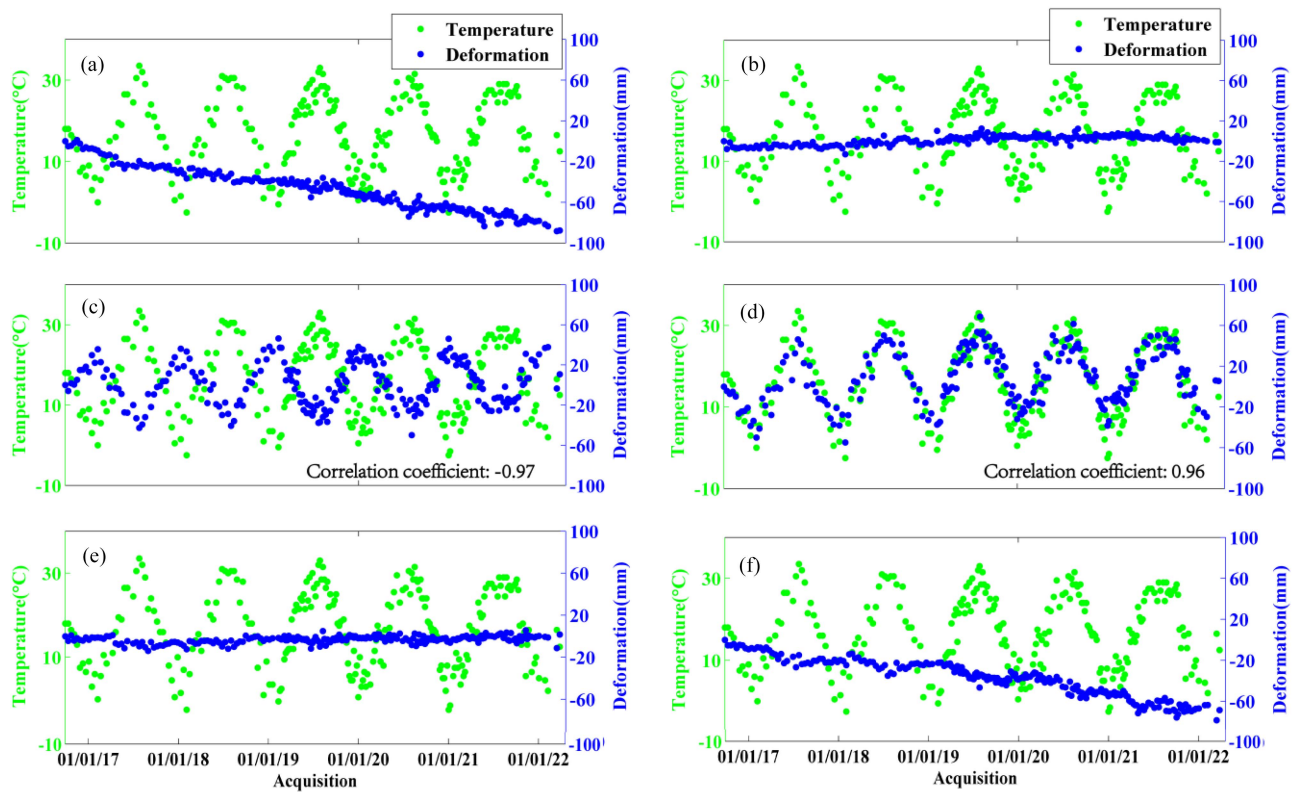


Fig. 7. Deformation time series. (a), (b), (c), (d), (e), and (f) correspond to points a, b, c, e, and f, respectively.

direction (see Fig. 7). This may be a critical factor for assessing the structural health of high-speed railway bridges. Fig. 7(c) clearly indicates the deformation characteristics and boundaries as well as the starting and ending positions of thermal expansion of the Nanjing Dashengguan Yangtze high-speed railway bridge.

In addition, at point P1, visible deformational characteristics were observed. Point P1 is located in Hexi of Nanjing, China, where the Yangtze River and Qinhuai River sediments are accumulated after the Pleistocene. Various sediments in the Hexi region alternate with each other, forming a relatively complex stratigraphic structure of silty clay, clay, sand, and silt. Groundwater exploitation changes in groundwater level, and

consolidation and compression of shallow strata can all cause land subsidence [44].

## V. APPLICATION TO XI'AN BUILDING DEFORMATION

Since the 1960s, the Xi'an area in China has experienced serious land subsidence as a result of the overexploitation of groundwater [45], [46], [47], which has caused serious societal and economic problems as the area has also become more urbanized. Severe ground subsidence poses a serious threat to buildings, affecting their lifespan and safety. While previous research has mainly focused on land subsidence and its mechanism analysis [45], [46], [47], we applied the

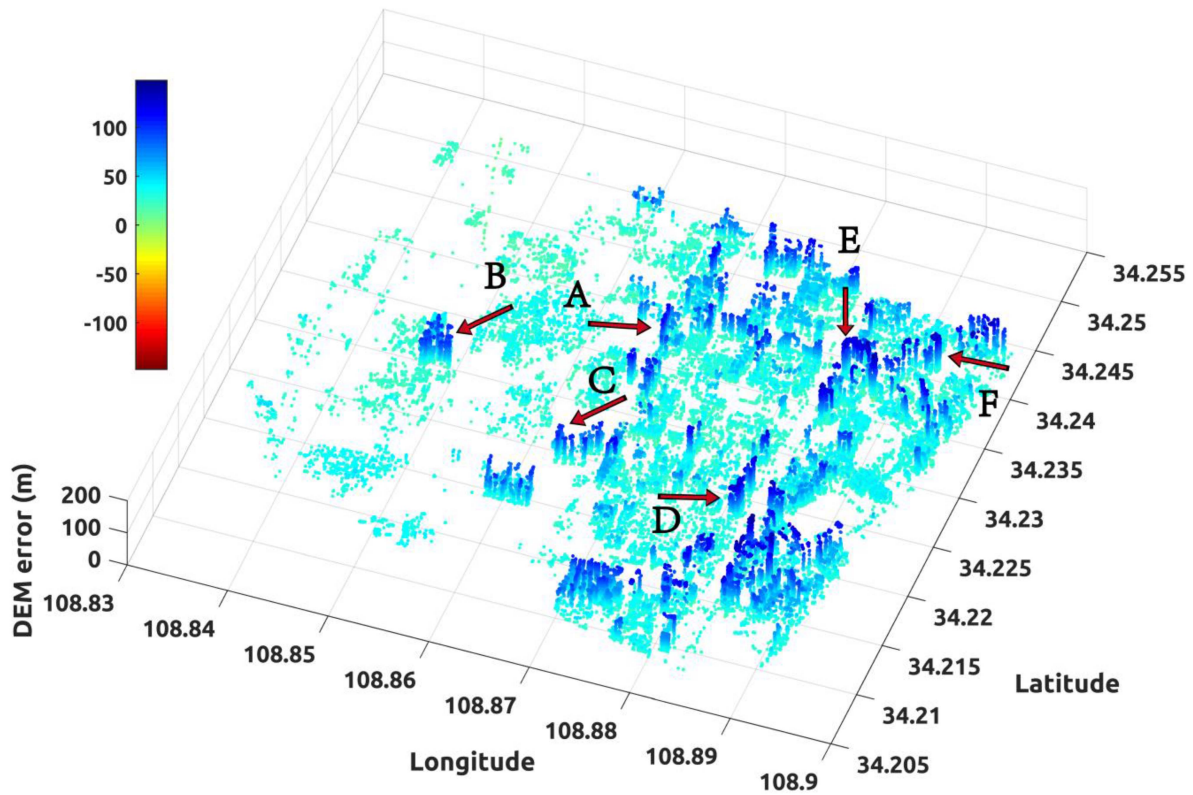


Fig. 8. Estimated DEM error.

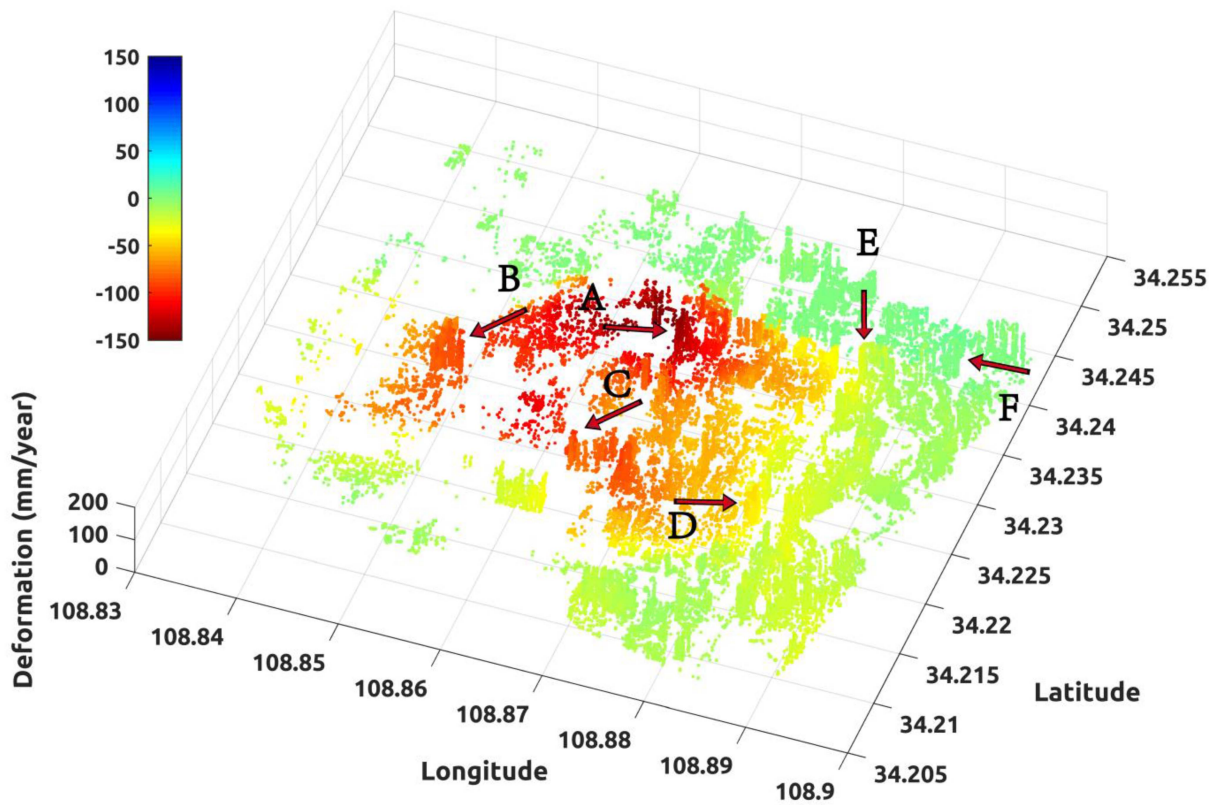


Fig. 9. Deformation rate. Points A–F are shown in Fig. 12.



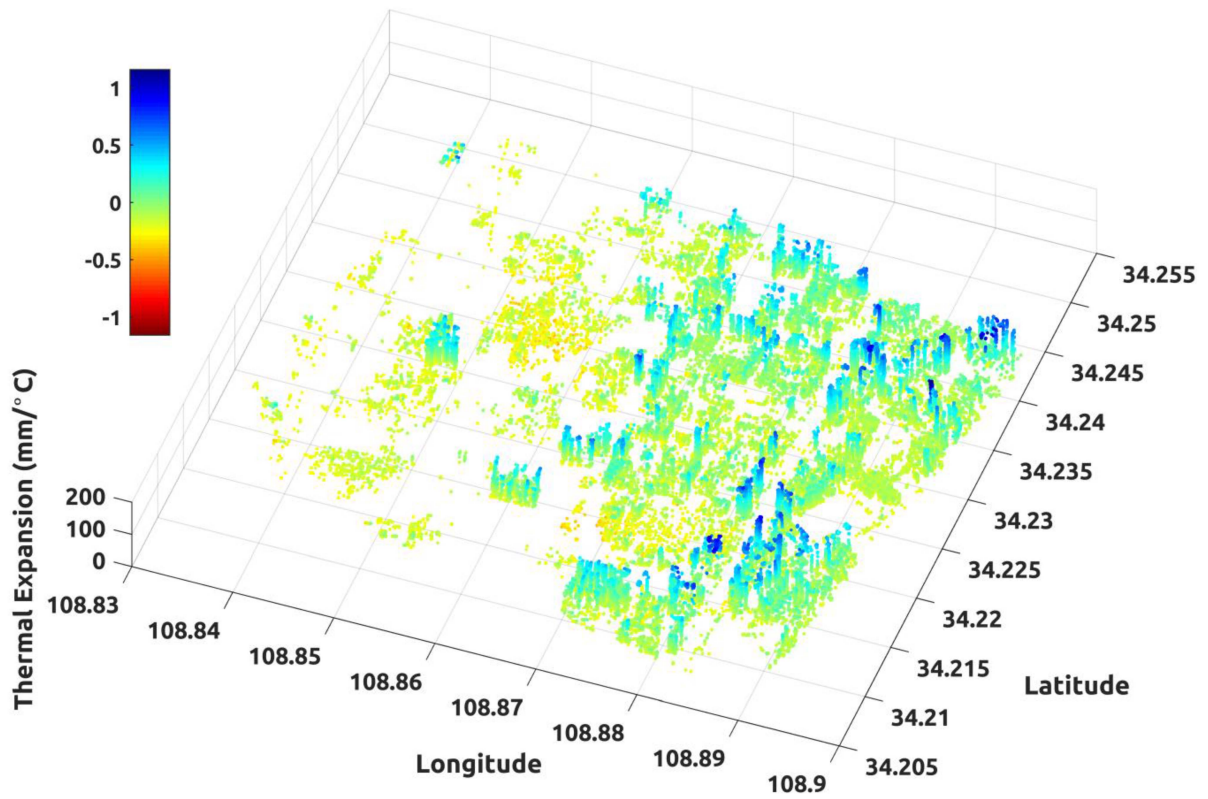


Fig. 10. Coefficient of thermal expansion.

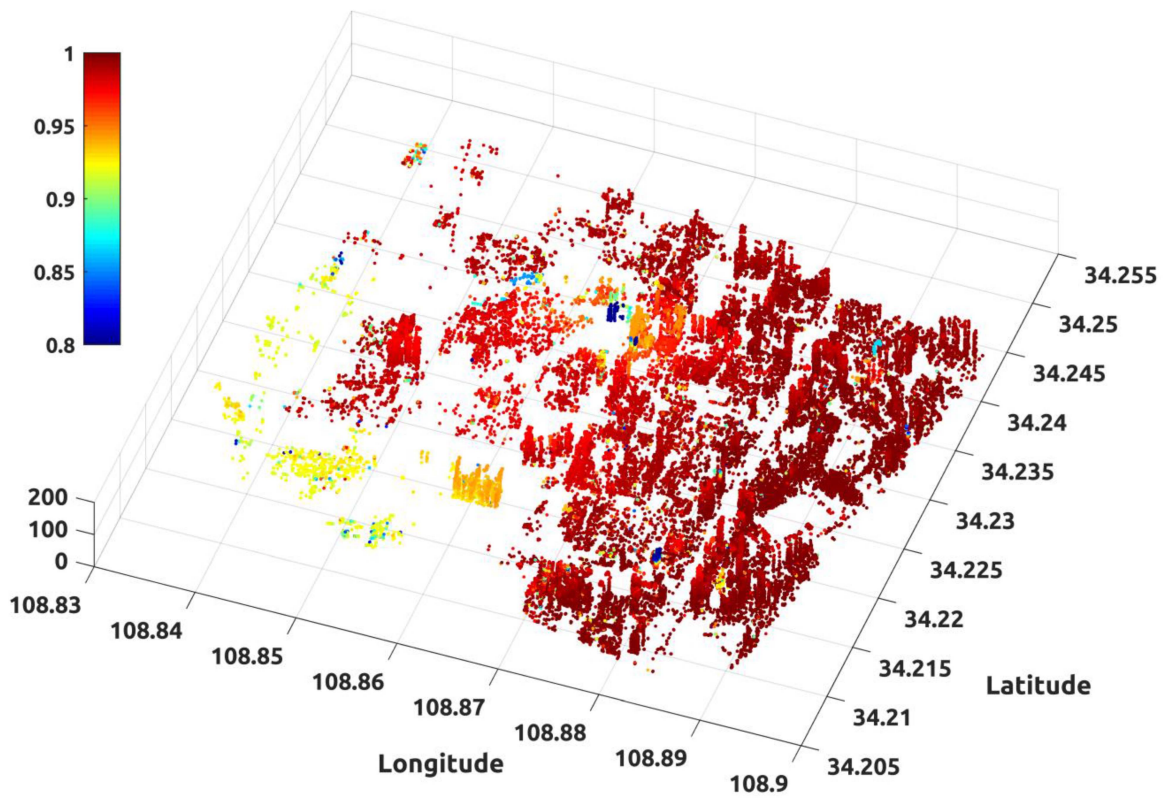


Fig. 11. Temporal coherence of residual.

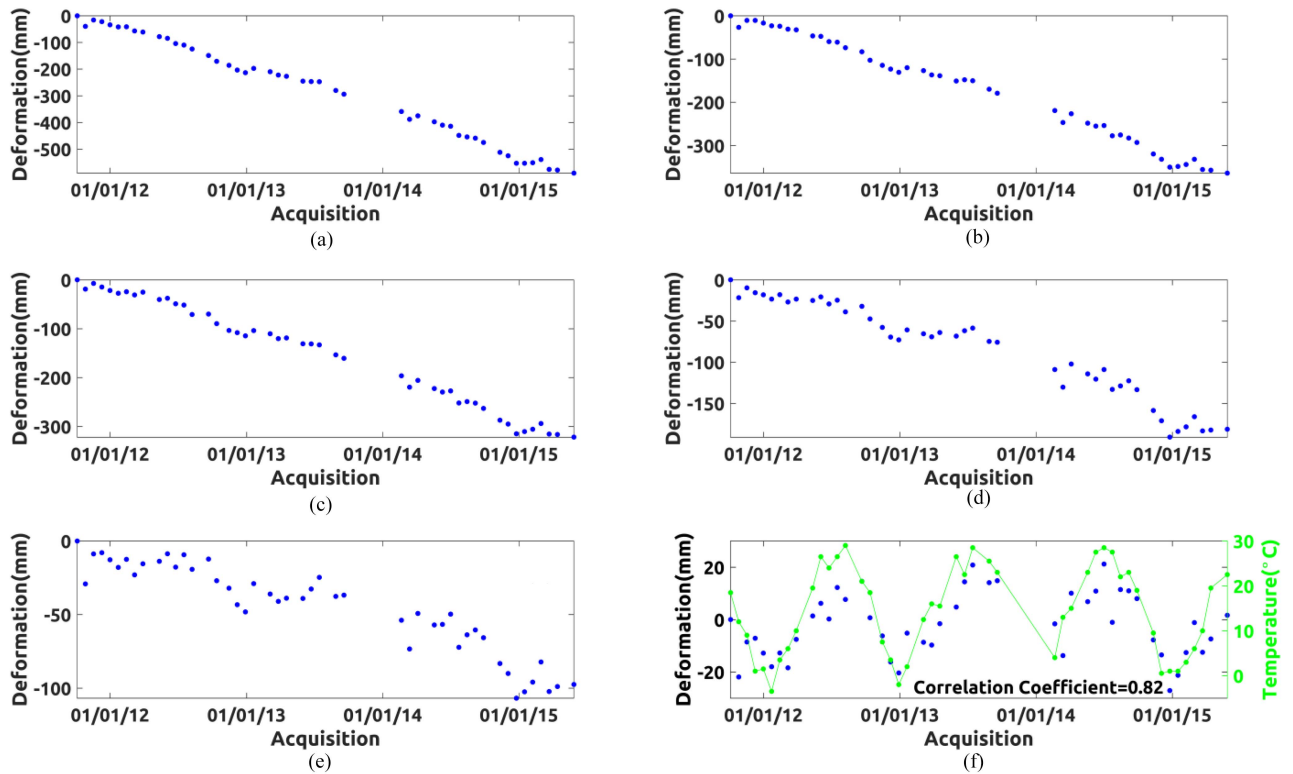


Fig. 12. Deformation time series. (a), (b), (c), (d), (e), and (f) correspond to points a, b, c, d, e, and f, respectively, in Figs. 8 and 9.

proposed method to map the infrastructure deformation in Xi'an, China.

In total, 46 TerraSAR-X data samples, collected between 2011 and 2015, were used to generate 200 interferograms. The amplitude deviation index was used to select 107 904 pixels [8]. To avoid isolating target points, we set the  $K$  nearest neighbor pixels (10 000) to generate redundant networks. Subsequently, we employed ambiguity detection to distinguish 28 308 622 reliable arcs. The NRO strategy with a threshold  $T_{\text{NRO}} = 5$  was used to optimize the reliable networks. Finally, we performed PhU for each interferogram. Figs. 8, 9, 10, and 11 show the DEM error, deformation rate, coefficient of thermal expansion, and temporal coherence of residual, respectively. Points a–f correspond to the deformation time series, as shown in Fig. 12.

The results indicate that buildings in land subsidence areas experienced severe deformation. The deformation characteristics of buildings in the nondeformation area were strongly correlated with temperature change. Infrastructural deformation may accelerate aging and increase potential risks.

## VI. CONCLUSION

In this study, a novel PhU network optimization algorithm is proposed, which aims to find optimal paths to improve the accuracy and efficiency of PhU. We suggest using a larger nearest neighbor pixel threshold to find reliable paths. Meanwhile, the NRO of each pixel in PhU networks is introduced to control network structure. It can improve the efficiency of PhU while ensuring accuracy. The Edgelist MCF PhU methods were used to test the reliability of optimized networks. We use high-resolution

TerraSAR-X data and low-resolution Sentinel-1A/B SAR to obtain deformation information. In discontinuous and irregular interferometric fringes, such as infrastructure and other complex scenarios, the proposed method is a potentially practical strategy.

## ACKNOWLEDGMENT

Sentinel-1A/B data were copyrighted by the European Space Agency. TerraSAR-X data were copyrighted by the European Space Agency.

## REFERENCES

- [1] R. Bürgmann, P. A. Rosen, and E. J. Fielding, "Synthetic aperture radar interferometry to measure earth's surface topography and its deformation," *Annu. Rev. Earth Planet. Sci.*, vol. 28, pp. 169–209, 2000.
- [2] S. Selvakumaran, S. Plank, C. Geiß, C. Rossi, and C. Middleton, "Remote monitoring to predict bridge scour failure using interferometric synthetic aperture radar (InSAR) stacking techniques," *Int. J. Appl. Earth Observ. Geoinf.*, vol. 73, pp. 463–470, 2018.
- [3] D. Perissin, Z. Wang, and H. Lin, "Shanghai subway tunnels and highways monitoring through Cosmo-SkyMed persistent scatterers," *ISPRS J. Photogramm. Remote Sens.*, vol. 73, pp. 58–67, 2012.
- [4] L. Chang, R. P. B. J. Dolvoet, and R. F. Hanssen, "Nationwide railway monitoring using satellite SAR interferometry," *IEEE J. Sel. Topics Appl. Earth Observ. Remote Sens.*, vol. 10, no. 2, pp. 596–604, Feb. 2017.
- [5] P. Ma et al., "Toward fine surveillance: A review of multitemporal interferometric synthetic aperture radar for infrastructure health monitoring," *IEEE Geosci. Remote Sens. Mag.*, vol. 10, no. 1, pp. 207–230, Mar. 2022.
- [6] M. Lazecky, I. Hlavacova, M. Bakon, J. J. Sousa, D. Perissin, and G. Patricio, "Bridge displacements monitoring using space-borne X-band SAR interferometry," *IEEE J. Sel. Topics Appl. Earth Observ. Remote Sens.*, vol. 10, no. 1, pp. 205–210, Jan. 2017.
- [7] X. Qin, X. Ding, M. Liao, L. Zhang, and C. Wang, "A bridge-tailored multi-temporal DInSAR approach for remote exploration of deformation characteristics and mechanisms of complexly structured bridges," *ISPRS J. Photogramm. Remote Sens.*, vol. 156, pp. 27–50, 2019.

- [8] A. Ferretti, C. Prati, and F. Rocca, "Permanent scatterers in SAR interferometry," *IEEE Trans. Geosci. Remote Sens.*, vol. 39, no. 1, pp. 8–20, Jan. 2001.
- [9] C. Werner, U. Wegmuller, T. Strozzi, and A. Wiesmann, "Interferometric point target analysis for deformation mapping," in *Proc. IEEE Int. Geosci. Remote Sens. Symp.*, 2003, vol. 7, pp. 4362–4364.
- [10] D. Perissin and T. Wang, "Repeat-pass SAR interferometry with partially coherent targets," *IEEE Trans. Geosci. Remote Sens.*, vol. 50, no. 1, pp. 271–280, Jan. 2012.
- [11] B. M. Kampes, "Displacement parameter estimation using permanent scatterer interferometry," Ph.D. dissertation, Delft Univ. Technol., Delft, The Netherlands, 2005.
- [12] L. Zhang, X. Ding, and Z. Lu, "Modeling PSInSAR time series without phase unwrapping," *IEEE Trans. Geosci. Remote Sens.*, vol. 49, no. 1, pp. 547–556, Jan. 2011.
- [13] O. Monserrat, M. Crosetto, M. Cuevas, and B. Crippa, "The thermal expansion component of persistent scatterer interferometry observations," *IEEE Geosci. Remote Sens. Lett.*, vol. 8, no. 5, pp. 864–868, Sep. 2011.
- [14] M. Costantini, S. Falco, F. Malvarosa, F. Minati, F. Trillo, and F. Vecchioli, "Persistent scatterer pair interferometry: Approach and application to COSMO-SkyMed SAR data," *IEEE J. Sel. Topics Appl. Earth Observ. Remote Sens.*, vol. 7, no. 7, pp. 2869–2879, Jul. 2014.
- [15] M. Costantini, "A novel phase unwrapping method based on network programming," *IEEE Trans. Geosci. Remote Sens.*, vol. 36, no. 3, pp. 813–821, May 1998.
- [16] C. W. Chen and H. A. Zebker, "Two-dimensional phase unwrapping with use of statistical models for cost functions in nonlinear optimization," *J. Opt. Soc. Amer. A*, vol. 18, pp. 338–351, 2001.
- [17] R. M. Goldstein, H. A. Zebker, and C. L. Werner, "Satellite radar interferometry: Two-dimensional phase unwrapping," *Radio Sci.*, vol. 23, no. 4, pp. 713–720, Jul./Aug. 1988.
- [18] W. Xu and I. Cumming, "A region-growing algorithm for InSAR phase unwrapping," *IEEE Trans. Geosci. Remote Sens.*, vol. 37, no. 1, pp. 124–134, Jan. 1999.
- [19] P. Ma and H. Lin, "Robust detection of single and double persistent scatterers in urban built environments," *IEEE Trans. Geosci. Remote Sens.*, vol. 54, no. 4, pp. 2124–2139, Apr. 2016.
- [20] W. Wu, J. Hu, Z. Du, J. Hou, W. Zheng, and J. Liu, "A network optimized ridge estimator for robust PSI parameter estimation and its application on deformation monitoring of urban area," *IEEE J. Sel. Topics Appl. Earth Observ. Remote Sens.*, vol. 14, pp. 5436–5452, 2021, doi: [10.1109/JSTARS.2021.3076452](https://doi.org/10.1109/JSTARS.2021.3076452).
- [21] W. Mao, S. Wang, B. Xu, Z. Li, and Y. Zhu, "An improved phase unwrapping method based on hierarchical networking and constrained adjustment," *Remote Sens.*, vol. 13, 2021, Art. no. 4193.
- [22] L. Zhou, H. Yu, Y. Lan, and M. Xing, "Artificial intelligence in interferometric synthetic aperture radar phase unwrapping: A review," *IEEE Geosci. Remote Sens. Mag.*, vol. 9, no. 2, pp. 10–28, Jun. 2021.
- [23] A. Pepe and R. Lanari, "On the extension of the minimum cost flow algorithm for phase unwrapping of multitemporal differential SAR interferograms," *IEEE Trans. Geosci. Remote Sens.*, vol. 44, no. 9, pp. 2374–2383, Sep. 2006.
- [24] C. Esch, J. Köhler, K. Gutjahr, and W.-D. Schuh, "One-step three-dimensional phase unwrapping approach based on small baseline subset interferograms," *Remote Sens.*, vol. 12, 2020, Art. no. 1473.
- [25] A. Hooper and H. A. Zebker, "Phase unwrapping in three dimensions with application to InSAR time series," *J. Opt. Soc. Amer. A*, vol. 24, pp. 2737–2747, 2007.
- [26] G. Fornaro, A. Paucillo, and D. Reale, "A null-space method for the phase unwrapping of multitemporal SAR interferometric stacks," *IEEE Trans. Geosci. Remote Sens.*, vol. 49, no. 6, pp. 2323–2334, Jun. 2011.
- [27] M. Caro Cuenca, A. J. Hooper, and R. F. Hanssen, "A new method for temporal phase unwrapping of persistent scatterers InSAR time series," *IEEE Trans. Geosci. Remote Sens.*, vol. 49, no. 11, pp. 4606–4615, Nov. 2011.
- [28] F. Liu and B. Pan, "A new 3-D minimum cost flow phase unwrapping algorithm based on closure phase," *IEEE Trans. Geosci. Remote Sens.*, vol. 58, no. 3, pp. 1857–1867, Mar. 2020.
- [29] B. Yang et al., "A multicomponent temporal coherence model for 3-D phase unwrapping in time-series InSAR of seasonal deformation areas," *Remote Sens.*, vol. 14, 2022, Art. no. 1080.
- [30] R. Li, X. Lv, J. Yuan, and J. Yao, "A triangle-oriented spatial-temporal phase unwrapping algorithm based on irrotational constraints for time-series InSAR," *IEEE Trans. Geosci. Remote Sens.*, vol. 57, no. 12, pp. 10263–10275, Dec. 2019.
- [31] H. Yu, Y. Lan, Z. Yuan, J. Xu, and H. Lee, "Phase unwrapping in InSAR: A review," *IEEE Geosci. Remote Sens. Mag.*, vol. 7, no. 1, pp. 40–58, Mar. 2019.
- [32] M. Costantini, F. Malvarosa, and F. Minati, "A general formulation for redundant integration of finite differences and phase unwrapping on a sparse multidimensional domain," *IEEE Trans. Geosci. Remote Sens.*, vol. 50, no. 3, pp. 758–768, Mar. 2012.
- [33] S. Wu, L. Zhang, X. Ding, and D. Perissin, "Pixel-wise MTInSAR estimator for integration of coherent point selection and unwrapped phase vector recovery," *IEEE Trans. Geosci. Remote Sens.*, vol. 57, no. 5, pp. 2659–2668, May 2019.
- [34] M. Jiang and A. M. Guarnieri, "Distributed scatterer interferometry with the refinement of spatiotemporal coherence," *IEEE Trans. Geosci. Remote Sens.*, vol. 58, no. 6, pp. 3977–3987, Jun. 2020.
- [35] W. Li, C. Zhao, B. Wang, and Q. Zhang, "L<sup>1</sup>-norm sparse 2-D phase unwrapping algorithm based on reliable redundant network," *IEEE Geosci. Remote Sens. Lett.*, vol. 19, pp. 1–5, 2022, Art. no. 8004605.
- [36] A. P. Shanker and H. Zebker, "Edgelist phase unwrapping algorithm for time series InSAR analysis," *J. Opt. Soc. Amer. A*, vol. 27, pp. 605–612, 2010.
- [37] L. Liu, C. Qu, and X. Shan, "An improved method of the finite-difference sparse phase unwrapping," *IEEE J. Sel. Topics Appl. Earth Observ. Remote Sens.*, vol. 14, pp. 4675–4683, 2021, doi: [10.1109/JSTARS.2021.3074393](https://doi.org/10.1109/JSTARS.2021.3074393).
- [38] Z.-F. Ma, M. Jiang, M. Khoshmanesh, and X. Cheng, "Time series phase unwrapping based on graph theory and compressed sensing," *IEEE Trans. Geosci. Remote Sens.*, vol. 60, pp. 1–12, 2022, Art. no. 5204412, doi: [10.1109/TGRS.2021.3066784](https://doi.org/10.1109/TGRS.2021.3066784).
- [39] Q. Zhang, J. Zhang, and D. Yue, *Advanced Theory and Application of Surveying Data*. Beijing, China: Surveying and Mapping Press, 2010.
- [40] A. R. Amiri-Simkooei, J. Asgari, F. Zangeneh-Nejad, and S. Zaminpardaz, "Basic concepts of optimization and design of geodetic networks," *J. Surv. Eng.*, vol. 138, pp. 172–183, 2012.
- [41] Q. Huang et al., "Displacement monitoring and health evaluation of two bridges using sentinel-1 SAR images," *Remote Sens.*, vol. 10, 2018, Art. no. 1714.
- [42] F. Chen, W. Zhou, C. Chen, and P. Ma, "Extended D-TomoSAR displacement monitoring for Nanjing (China) city built structure using high-resolution TerraSAR/TanDEM-X and COSMO SkyMed SAR data," *Remote Sens.*, vol. 11, 2019, Art. no. 2623.
- [43] P. Berardino, G. Fornaro, R. Lanari, and E. Sansosti, "A new algorithm for surface deformation monitoring based on small baseline differential SAR interferograms," *IEEE Trans. Geosci. Remote Sens.*, vol. 40, no. 11, pp. 2375–2383, Nov. 2002.
- [44] B. Zhu, F. Yao, J. Sun, and X. Wang, "Attribution analysis on land subsidence feature in Hexi area of Nanjing by InSAR and geological data[J]," *Geomatics Inf. Sci. Wuhan Univ.*, vol. 45, no. 3, pp. 442–450, 2020.
- [45] B. Wang, C. Zhao, Q. Zhang, and M. Peng, "Sequential InSAR time series deformation monitoring of land subsidence and rebound in Xi'an, China," *Remote Sens.*, vol. 11, 2019, Art. no. 2854.
- [46] B. Wang, C. Zhao, Q. Zhang, Z. Lu, and A. Pepe, "Long-term continuously updated deformation time series from multisensor InSAR in Xi'an, China from 2007 to 2021," *IEEE J. Sel. Topics Appl. Earth Observ. Remote Sens.*, vol. 14, pp. 7297–7309, 2021, doi: [10.1109/JSTARS.2021.3096996](https://doi.org/10.1109/JSTARS.2021.3096996).
- [47] G. Li, C. Zhao, B. Wang, M. Peng, and L. Bai, "Evolution of spatiotemporal ground deformation over 30 years in Xi'an, China, with multi-sensor SAR interferometry," *J. Hydrol.*, vol. 616, 2023, Art. no. 128764.



**Baohang Wang** received the M.S. and Ph.D. degrees in geodesy and surveying engineering from Chang'an University, Xi'an, China, in 2015 and 2022, respectively.

He is currently a Lecturer of geodesy and surveying engineering with the College of Geography and Oceanography, Minjiang University, Fuzhou, China. His research interests include the development of different InSAR methods, including spatiotemporal phase optimization, phase unwrapping, and SAR/InSAR deformation time series updating for artificial infrastructure facilities, land subsidence, and landslide.



**Chaoying Zhao** (Senior Member, IEEE) received the M.S. and Ph.D. degrees in geodesy and surveying engineering from Chang'an University, Xi'an, China, in 2002 and 2009, respectively.

He is currently a Professor of geodesy and survey engineering with Chang'an University. He is specialized in the development of InSAR methods, including dynamic SAR/InSAR data processing with the sequential least squares, large gradient surface deformation with SAR offset tracking method, and their applications in geohazards identification, monitoring, and mechanism explanations, including land subsidence, ground fissures, landslide, and mining-induced collapse.



**Wenhong Li** received the M.S. degree in surveying and mapping engineering from Chang'an University, Xi'an, China, in 2021.

He is with the Cooperative Centre for Geological Surveys in Central and Western Asia, Xi'an Center of Geological Survey, China Geological Survey, Xi'an, China. His research interests include InSAR data processing and applications, as well as geoscience big data analysis.



**Qin Zhang** (Member, IEEE) received the Ph.D. degree in geodesy from Wuhan University, Wuhan, China, in 2002.

She is currently a Professor of geodesy and survey engineering with Chang'an University, Xi'an, China. She is currently working on the high-precision geodetic data processing and algorithm development, including GNSS and InSAR, and the monitoring and early forecast on geohazards, including land subsidence, ground fissures, and landslide.



**Guangrong Li** was born in Yibin, China. He received the B.S. and M.S. degrees in geodesy and surveying engineering in 2020 and 2023, respectively, from Chang'an University, Xi'an, China, where he is currently working toward the Ph.D. degree.

His research interests include InSAR algorithm development, dynamic monitoring of surface deformation and height changes, and coupling of groundwater and ground subsidence.



**Ya Kang** received the M.S. and Ph.D. degrees in geodesy and surveying engineering from Chang'an University, Xi'an, China, in 2016 and 2020, respectively.

He is currently a Lecturer with the Nanjing University of Posts and Telecommunications, Nanjing, China. His research interests include InSAR processing, landslide detecting and monitoring with InSAR, and geophysical modeling of landslide.



**Chengsheng Yang** received the M.S. and Ph.D. degrees in geodesy and surveying engineering from Chang'an University, Xi'an, China, in 2008 and 2012, respectively.

He is currently a Professor with Chang'an University. His current research interests include InSAR data processing and atmospheric effect mitigation.



**Shouzhu Zheng** received the Ph.D. degree in surveying and mapping from Tongji University, Shanghai, China, in 2021.

He is currently an Assistant Professor with the College of Geography and Oceanography, Minjiang University, Fuzhou, China. His research interests include photogrammetry and remote sensing, and video object detection and tracking.